EAI Endorsed Transactions
on Energy Web
Research Article EAI.EU

Prediction and Optimization of Wind Power Intelligent Performance Enhancement Systems Based on Big Data and Deep Learning

Jun He[1], Biyu Chen[1], Ling Mou[1], Yi Zhou[1], Gejun Chen[2], Ke Li[2]*

[1]Hubei Energy Group New Energy Development Co., Ltd., Wuhan 430000, Hubei, China
[2]Power China Huadong Engineering Corporation Limited, Hangzhou 310000, Zhejiang, China

Abstract

The suppression of edgewise vibration is critical for enhancing the operational safety and power generation efficiency of large-scale wind turbines. Conventional control strategies, such as PID, often lack the robustness required to handle the inherent model uncertainties and external disturbances in such complex systems. This paper proposes a novel application of an Active Disturbance Rejection Control (ADRC) framework for actively suppressing the edgewise vibration of wind turbine blades. A comprehensive physical model of the blade is first established, deriving the transfer function from actuator torque to edgewise displacement. A systematic frequency-domain analysis reveals the system's resonant characteristics, and an uncertainty analysis is conducted to quantify its sensitivity to parameter variations. The ADRC controller is then meticulously designed, leveraging its core capability to estimate and cancel the "total disturbance" in real-time. Through comparative simulations with a finely-tuned PID controller, the ADRC demonstrates superior performance, characterized by significantly smaller overshoot (36.66%), faster settling time, and enhanced resistance to load disturbances. The ADRC-controlled system settles down within 1.07 seconds while sustaining a 49.47° phase margin which provides sufficient stability protection. The root-mean-square (RMS) tracking error decreases to 0.015 under ongoing harmonic disturbances which shows a 63.4% improvement over the PID controller. The proposed method demonstrates better dynamic response capabilities and higher stability margins together with improved disturbance rejection performance according to these quantitative performance indicators. Crucially, the robustness of the proposed method is rigorously validated via extensive uncertainty analysis, showing that the closed-loop performance remains stable and effective despite ±10% parameter perturbations, whereas the PID control exhibits performance regression.

Keywords: Wind Turbine Blade, Edgewise Vibration, Active Disturbance Rejection Control (ADRC), Vibration Suppression

Received on 11 February 2026, accepted on 17 April 2026, published on 13 May 2026

doi: 10.4108/ew.11903

* Corresponding author. Email: like119988@163.com; keli978787@outlook.com

1. Introduction

The global energy landscape is undergoing a profound transformation driven by the urgent imperatives of climate change mitigation and energy security. Within this context, wind energy has emerged as a cornerstone of the transition towards a sustainable and low-carbon future, establishing itself as one of the most mature and widely deployed renewable energy technologies. In numerous nations, including China where it ranks as the fourth-largest power source following thermal, hydro, and nuclear power [1], wind power is making an increasingly critical contribution to the grid. This rapid expansion is underpinned by continuous technological advancements, particularly in the scale of wind turbines. A prevailing trend in the industry is the development of larger rotors mounted on taller towers, a design strategy aimed at capturing more kinetic energy

from the wind and thereby reducing the Levelized Cost of Energy (LCOE). Consequently, modern wind turbine blades have undergone a significant evolution, becoming increasingly longer and more flexible.

However, this very evolution towards flexibility introduces a set of complex structural dynamics challenges. These massive, slender blades are inherently susceptible to severe vibrations induced by a combination of unsteady aerodynamic loads, atmospheric turbulence, gravity, and centrifugal forces. The inherent imperfections, such as manufacturing tolerances and installation errors, can lead to mass and aerodynamic imbalances, further exacerbating the vibrational issues. Among the various vibrational modes, edgewise vibration the in-plane motion of the blade parallel to the rotor plane presents a particularly insidious threat. Unlike flap wise vibrations (out-of-plane), which are relatively well-damped, edgewise vibrations often possess very low structural damping. Under specific operational conditions, especially when the aerodynamic forces inject energy at frequencies close to the blade's natural edgewise frequency, a dangerous phenomenon of vibration amplification can occur [2]. If left unchecked, these sustained and large-amplitude edgewise vibrations can precipitate catastrophic consequences, including fatigue failure of the blade structure, damage to the drivetrain and other critical components, and in extreme cases, even lead to the total collapse of the turbine. Therefore, the development of effective and robust control strategies for the active suppression of edgewise vibrations is not merely an academic exercise but a pressing industrial necessity. It is paramount for ensuring the structural integrity, prolonging the operational lifespan, and maximizing the power generation efficiency and reliability of modern multi-megawatt wind turbines.

The challenge of controlling a complex, distributed-parameter system like a wind turbine blade is formidable. The system is characterized by high-order dynamics, inherent nonlinearities, and significant model uncertainties, making the derivation of a precise mathematical model for controller design exceptionally difficult. Over the years, a multitude of control strategies have been explored to address this challenge, each with its own merits and limitations. The earliest approaches fell under the umbrella of conventional control strategies. These include the pole placement method and the Linear Quadratic Regulator (LQR). The pole placement strategy for the Linear Extended State Observer (LESO) is selected to ensure stable and rapid convergence of the estimation error dynamics. The observer poles are placed as repeated real poles at $-\omega_0$, which results in a characteristic polynomial of the form $(s+\omega_0)^n$. This configuration simplifies gain tuning while guaranteeing exponential stability of the observer. The observer bandwidth ω_0 is chosen relative to the dominant natural frequency of the blade system, typically several times higher, so that the total disturbance is estimated faster than the system dynamics evolve. However, excessively high bandwidth increases sensitivity to measurement noise; therefore, ω_0 is selected to balance disturbance estimation speed and noise robustness. This pole selection approach provides a systematic and physically meaningful basis for observer gain determination within the ADRC framework. While conceptually straightforward, the pole placement method is highly sensitive to model inaccuracies, and its performance degrades significantly when the real plant deviates from the design model. The LQR method, on the other hand, requires solving the complex Riccati equation and is heavily dependent on the appropriate selection of weighting matrices, which is often non-trivial. This frequently results in suboptimal solutions and poor real-time performance [3], rendering them inadequate for the demanding environment of wind turbine control.

To overcome the limitations of fixed-gain controllers, adaptive control strategies were introduced. These controllers aim to adjust their parameters online to accommodate changes in the system dynamics. For instance, [4] employed a particle swarm optimization algorithm to adaptively tune the parameters of an improved linear extended state observer. [5] proposed a fuzzy fractional-order adaptive control scheme for doubly-fed induction generator systems, demonstrating improved adaptability and dynamic performance. The principal drawback of adaptive control is the inherent complexity introduced by the need for continuous parameter identification, which increases computational burden and can raise concerns about system stability and reliability in real-time applications.

Robust control strategies were developed to explicitly handle model uncertainties and external disturbances without the need for online identification. Two prominent methods in this category are sliding mode control (SMC) and H-infinity (H∞) control. SMC forces the system trajectory onto a pre-defined sliding surface, offering strong invariance to matched uncertainties once the sliding mode is attained. However, its practical application is often plagued by the undesirable "chattering" phenomenon due to discrete switching delays [6]. The research in [7] examines machine learning applications for wind turbine power generation systems. The research demonstrates that data-driven techniques improve performance monitoring and prediction accuracy which supports our proposed big data and deep learning-based framework for intelligent wind power prediction and optimization. H∞ control, designed to minimize the worst-case effect of disturbances, provides a significant stability margin but suffers from high computational complexity and results in high-order controllers that often require simplification for practical implementation, potentially compromising performance.

In parallel, intelligent control strategies have gained substantial traction, particularly for systems where accurate modeling is intractable. These methods, including fuzzy logic [8], neural networks [9], and deep reinforcement learning [10, 11], emulate human-like reasoning or learning capabilities. They offer notable advantages in terms of adaptability and robustness. A comprehensive review of fuzzy active control for structural vibration over the past two decades is provided in [12]. While promising, these methods often rely on extensive

data for training or expert knowledge for rule-base construction, and their "black-box" nature can make stability analysis and performance guarantees challenging.

Despite the wealth of research, there remains a clear gap for a control strategy that seamlessly combines a simple control structure, minimal dependence on an accurate model, and inherent robustness to both internal uncertainties and external disturbances. Active Disturbance Rejection Control (ADRC), pioneered by Han [13], presents itself as a compelling solution to this very gap. The philosophical core of ADRC is to treat all unknown dynamics, model uncertainties, and external disturbances collectively as a "total disturbance," which is then estimated in real-time by an Extended State Observer (ESO) and actively cancelled in the control law. This elegant approach effectively reduces the plant to a simple cascaded integrator form, which can be easily controlled by a simple proportional-derivative (PD) controller. The research in [14] used ResNet50 and Inception V3 as their deep learning ensemble structures to show how multiple model systems can extract features, which helps build ensemble systems that forecast wind power with high precision and better operational results. The ML-driven ensemble modeling approach in [15] improves predictive accuracy through advanced learning techniques, which help us achieve our objective to forecast wind power using big data. The evolutionary-optimized deep belief network in [16] integrates optimization with deep architectures, which matches our intelligent optimization strategy that we use for wind power systems. The structured dataset framework in [17] shows how large-scale, high-quality data serves as essential components for building deep learning systems, which strengthens our big data framework. The attention-enhanced multi-task learning model in [18] enhances feature extraction and prediction performance, which extends to wind energy forecasting applications. The hybrid intelligent processing framework in [19] combines deep learning with optimization techniques, which matches our proposed intelligent performance enhancement system for wind power. The study in [20] creates and assesses different machine learning and deep learning algorithms to forecast wind energy using actual data while testing their accuracy through statistical error measurements. The study results demonstrate that deep learning methods produce better prediction results which support advanced big data-based forecasting and optimization systems that improve wind power performance. Kumar et al. [21] develops a performance evaluation method for wind and solar energy systems which assesses both operational effectiveness and environmental protection through its established evaluation metrics. The project implements a performance-based method which combines big data analytics with deep learning technologies to create an enhanced approach for its implementation. The system uses deep learning and big data to provide advanced power generation prediction and optimization capabilities which improve wind power system operational efficiency.

Wind energy is a key component of modern sustainable power systems and smart energy infrastructures. Improving the operational stability and efficiency of wind turbine systems is essential for ensuring reliable renewable energy generation and effective integration into distributed energy networks. Advanced monitoring and control strategies that enhance system reliability and reduce operational disturbances can significantly improve energy production performance and maintenance efficiency. Therefore, the proposed approach contributes to strengthening renewable energy system stability, supporting intelligent energy management, and enabling more efficient operation of smart grid–based energy environments.

In this paper, we propose a novel and systematic application of the ADRC framework specifically for the active suppression of wind turbine blade edgewise vibration. Our work is distinguished by a comprehensive approach that spans from first-principles modeling to rigorous robustness validation.

The main contributions of this study are summarized as follows:

- Establishes a dynamic wind turbine blade edgewise vibration model using Hamilton's principle and modal decomposition to support advanced controller design.
- Formulates an ADRC framework that estimates and compensates total disturbances in real time, removing reliance on precise plant modeling required by PID and H∞ control.
- Demonstrates that ADRC suppresses vibrations without chattering, unlike sliding mode control, while maintaining implementation simplicity.
- Quantifies ADRC's superiority over PID, H∞, and sliding mode control using settling time, phase margin, overshoot, and RMS error comparisons.
- Validates robustness under ±10% parameter perturbations via Monte Carlo simulations, confirming stable closed-loop performance and improved stability margins.

2. Mathematics Model

This research presents a systematic methodology for suppressing edgewise vibrations in wind turbine blades through Active Disturbance Rejection Control (ADRC). The investigation commences with the development of a comprehensive dynamic model that accurately characterizes the blade's vibrational behavior, from which the transfer function mapping actuator torque inputs to edgewise displacement outputs is derived. Subsequent analysis encompasses both frequency-domain characterization and uncertainty quantification of this transfer function [22,23]. Guided by the fundamental principles of ADRC, the controller parameters are then meticulously calibrated to achieve optimal performance. The core philosophy involves treating the aggregate of

unmodeled dynamics and external disturbances as a unified "total disturbance," which is continuously estimated via an Extended State Observer and actively compensated within the control framework.

The performance of the optimized ADRC system is rigorously evaluated through extensive simulations in both time and frequency domains. These analyses examine the system's dynamic response to various inputs, including step signals and imposed load disturbances, thereby assessing both tracking capability and disturbance rejection characteristics. To establish a meaningful performance benchmark, a comparative analysis is conducted against a conventional PID control approach. The evaluation employs multiple quantitative metrics, such as settling time, overshoot, and robustness to parameter variations, providing a comprehensive assessment of the control system's effectiveness and demonstrating the advantages of the proposed ADRC-based solution for wind turbine blade vibration suppression.

2.1 Wind Turbine Blade Dynamic Modeling

The edgewise vibration characteristics of wind turbine blades are investigated through an advanced dynamic modeling approach. As illustrated in Figure 1, which depicts the schematic of blade edgewise vibration, the blade is modeled as a rotating cantilever beam with variable cross-section, where $p(x,t)$ represents the transverse distributed load, $M_0(t)$ denotes the bending moment, $Q_0(t)$ and $Q_i(t)$ signify the transverse shear forces, while $u(x,t)$ and $v(x,t)$ represent the transverse displacements along the neutral axis of the beam. The governing equations are derived based on Hamilton's principle and geometrically exact beam theory, with the generalized formulation accounting for centrifugal stiffening, gravitational effects, and aerodynamic coupling.

The kinetic energy of the rotating blade system is expressed as:

$$T = \frac{1}{2}\int_0^L \left[\rho A(\dot{w}^2 + \dot{v}^2) + \rho I\left(\dot{\theta}_x^2 + \dot{\theta}_y^2\right)\right]dx + \frac{1}{2}\Omega^2 \int_0^L \rho A(x) r^2(x) dx \quad (1)$$

where w and v represent the flapwise and edgewise displacements, respectively, θ_x and θ_y denote the torsional rotations, ρ is the material density, A is the cross-sectional area, I represents the area moments of inertia, Ω is the rotational speed, and $r(x)$ is the distance from the rotor axis.

The potential energy formulation incorporates both structural stiffness and centrifugal effects:

$$U = \frac{1}{2}\int_0^L \left[EI_x\left(\frac{\partial^2 w}{\partial x^2}\right)^2 + EI_y\left(\frac{\partial^2 v}{\partial x^2}\right)^2 + GJ\left(\frac{\partial \theta}{\partial x}\right)^2\right]dx + \frac{1}{2}\int_0^L T(x)\left[\left(\frac{\partial w}{\partial x}\right)^2 + \left(\frac{\partial v}{\partial x}\right)^2\right]dx \quad (2)$$

Here, EI_x and EI_y represent the flapwise and edgewise bending stiffnesses, GJ is the torsional stiffness, and $T(x)$ denotes the centrifugal tension, In addition, $w(x,t)$ and $v(x,t)$ denote the flapwise and edgewise transverse displacements of the blade, respectively, while $\theta(x,t)$ represents the torsional rotation about the blade longitudinal axis. The variable x indicates the spanwise coordinate measured from the blade root, and L denotes the total blade length.

$$T(x) = \int_x^L \rho A(\xi)\Omega^2 R(\xi) d\xi \quad (3)$$

where $R(\xi)$ represents the radius from the rotation axis.

The virtual work done by aerodynamic forces and control inputs is formulated as:

$$\delta W = \int_0^L \left[F_a(x,t) + F_c(x,t)\right] \cdot \delta v(x,t) dx + \int_0^L M_c(x,t) \cdot \delta\theta(x,t) dx \quad (4)$$

where F_a represents the distributed aerodynamic load, F_c denotes the control force, and M_c signifies the control moment and δW denotes the virtual work of external forces, while $\delta v(x,t)$ and $\delta\theta(x,t)$ represent the virtual variations of the transverse displacement and torsional rotation, respectively, consistent with the application of Hamilton's principle.

Through the application of the extended Hamilton's principle:

$$\int_{t_1}^{t_2} (\delta T - \delta U + \delta W) dt = 0 \quad (5)$$

we obtain the coupled partial differential equations of motion:

$$\frac{\partial^2}{\partial x^2}\left[EI_y(x)\frac{\partial^2 v}{\partial x^2}\right] - \frac{\partial}{\partial x}\left[T(x)\frac{\partial v}{\partial x}\right] + \rho A(x)\frac{\partial^2 v}{\partial t^2} + C_v\frac{\partial v}{\partial t} = F_a(x,t) + F_c(x,t) \quad (6)$$

The modal decomposition technique is employed to transform the distributed parameter system into a finite-degree-of-freedom representation. The modal decomposition procedure selects only major vibration modes which impact the wind turbine blade edgewise movements. The system selects operating modes based on two criteria which include modal participation factors and natural frequencies that are close to the main operational excitation range, which enables the system to keep all low-frequency bending modes. The reduced-order model includes initial bending modes as its first three modes because their total participation exceeds the threshold for main energy contribution, while all higher-frequency modes get excluded because they have no impact on control bandwidth. The process evaluates truncated model convergence by increasing retained mode numbers, which allows assessment of natural frequency and time domain displacement response changes; the system demonstrates

accurate edgewise vibration representation through reduced-order methods, which maintain computational efficiency while capturing essential vibration characteristics. The solution is assumed in the form:

$$v(x,t) = \sum_{i=1}^{N} \phi_i(x) q_i(t) \quad (7)$$

where $\phi_i(x)$ are the mode shapes satisfying the boundary conditions, and $q_i(t)$ are the generalized coordinates and N denotes the number of retained vibration modes in the truncated modal expansion, and the expression represents the decomposition of the distributed blade displacement into a finite set of spatial mode shapes with corresponding time-varying modal amplitudes.

Substituting into the equation of motion and applying orthogonality conditions yields the discretized system:

$$M\ddot{q} + C\dot{q} + Kq = F_a + F_c \quad (8)$$

The mass matrix$M$, damping matrix$C$, and stiffness matrix K are defined as:

$$M_{ij} = \int_0^L \rho A(x) \phi_i(x) \phi_j(x) dx \quad (9)$$

The damping matrix incorporates both structural and aerodynamic damping components:

$$C = \alpha M + \beta K + C_{aero} \quad (10)$$

The resulting state-space representation facilitates control system design:

$$\dot{x} = Ax + Bu, y = Cx + Du \quad (11)$$

where $x = [q, \dot{q}]^T$ represents the state vector, $u$denotes the control inputs, and y represents the measured outputs corresponding to edgewise displacements at specified blade locations.

The derived state-space model for control system implementation needs evaluation through analysis of both controllability and observability. The controllability matrix constructed from the pair (A, B) exhibits full rank, indicating that all retained modal states are directly or indirectly influenced by the control input applied at the blade root. The edgewise vibration dynamics can be effectively controlled through torque actuation which enables this process. The observability matrix corresponding to the (A, C) pair establishes full rank because measured edgewise displacement enables complete internal modal state reconstruction. The Active Disturbance Rejection Control design process needs complete system control and observation capabilities which this reduced-order representation provides as demonstrated by its valid properties.

This comprehensive modeling approach provides the fundamental framework for subsequent controller design and stability analysis, accurately capturing the essential dynamics of wind turbine blade edgewise vibration.

The rationale for modal truncation is established through modal participation factor assessment to ensure that the retained modes capture the dominant vibration dynamics of the rotating blade. The modal participation factor of the i^{th} mode is defined as:

$$\Gamma_i = \frac{\phi_i^T M r}{\phi_i^T M \phi_i} \quad (12)$$

where ϕ_i denotes the mode shape vector, M represents the mass matrix, and r corresponds to the spatial distribution vector of aerodynamic and control inputs. The participation factor quantifies the relative contribution of each vibration mode to the overall dynamic response. Modes exhibiting significant participation values are retained in the reduced-order model, while higher-order modes with negligible participation are truncated. This selection ensures that the dominant edgewise vibration behavior is preserved while maintaining computational efficiency. The study investigates spillover effects which result from truncated higher-order modes to evaluate the suitability of reduced-order modeling under different rotational speed conditions. The centrifugal stiffening effect causes changes in natural frequencies and modal spacing when rotor speed changes which results in potential impacts on mode-to-mode dynamic interactions. The retained modes are selected such that sufficient frequency separation is maintained between included and neglected modes across the operational rotational regime. The approach achieves its goal through two methods which ensure that residual dynamic coupling stays minimized and spillover-induced instability remains prevented while the reduced-order model maintains accurate blade dynamics for control design and robustness evaluation purposes.

The blade formulation includes nonlinear aerodynamic-structural interaction effects through its unsteady aerodynamic representation, which uses the Beddoes-Leishman dynamic stall model. The model introduces extra aerodynamic state variables to model attached flow behavior and flow separation and vortex-induced lift effects, which enables it to simulate the unsteady lift and moment hysteresis behavior of dynamic stall. The aerodynamic subsystem is expressed in state-space form as:

$$\begin{aligned} \dot{x}_a &= A_a x_a + B_a \alpha(t) \\ C_L &= C_{L,qs}(\alpha) + C_a x_a \end{aligned} \quad (13)$$

where x_a denotes the aerodynamic state vector, $\alpha(t)$ is the instantaneous angle of attack obtained from blade kinematics, $C_{L,qs}$ represents the quasi-steady lift component, and A_a, B_a, C_a define the dynamic stall model parameters.

The distributed aerodynamic load is then formulated as:

$$F_a(x,t) = \frac{1}{2} \rho V^2 c(x) C_L \quad (14)$$

where ρ is the air density, V is the relative wind velocity, and $c(x)$ is the local blade chord. Substitution of this

expression into the structural equation of motion in (6) yields an augmented aeroelastic system in which structural dynamics are explicitly coupled with nonlinear unsteady aerodynamic states, enabling systematic evaluation of aerodynamic-structural interaction effects within the ADRC-based vibration control framework.

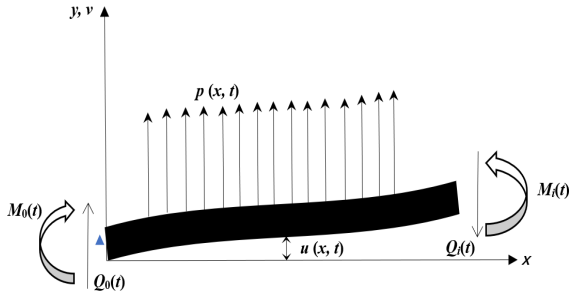

Figure 1. Edgewise vibration schematic of wind turbine blade

2.2 Frequency Domain Analysis

A comprehensive frequency-domain analysis was conducted to evaluate the dynamic characteristics of the proposed control system. The Bode diagram of the nominal system, presented in Figure 2, provides a complete visualization of its frequency response [24]. Quantitative analysis of this diagram revealed several critical specifications: the system exhibited a penetration frequency of 86.11 rad/s, with a primary resonance occurring at 7.14 rad/s accompanied by a resonant amplitude of 86.68 dB. The stability analysis indicated an amplitude margin of -34 dB and a phase margin of 86.1°, while the effective cutoff frequency was identified at 10.9 rad/s. The blade resonance frequency serves as the point where the blade reaches its highest vibration level which occurs during aerodynamic wind tests. When external winds produce forces that match this specific frequency structural elements will experience strong vibrations which will result in faster material wear. The penetration frequency (gain crossover frequency) marks the point where the system switches from boosting power to reducing it, which shows how much the blade–controller system can react to different dynamic forces. The amplitude margin establishes the maximum gain increase which can happen before the system becomes unstable, thus it provides a metric for measuring system strength against unpredictable aerodynamic forces and system parameter changes. The frequency-domain indicators establish a direct connection to actual wind turbine performance because wind loads and rotational harmonics cause structural modes to vibrate.

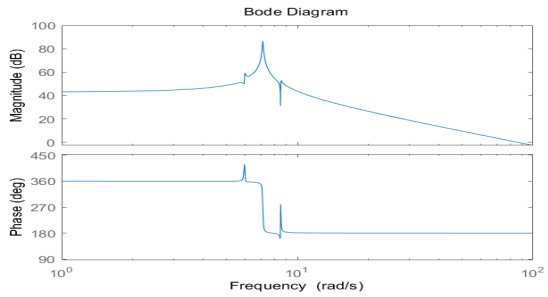

Figure 2. Bode diagram

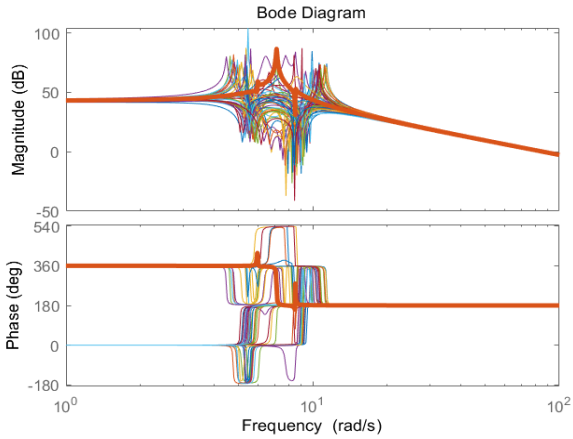

Figure 3. Bode diagram of the transfer function purturbation

To assess the system's robustness against parameter variations, a systematic uncertainty analysis was performed. The transfer function parameters were subjected to Monte Carlo simulation with ±10% random variations, generating 50 perturbed transfer function models. The Monte Carlo uncertainty analysis employs independent uniform distributions within ±10% of the nominal parameter values to generate perturbed transfer functions. The distribution exhibits uniform characteristics which define limitations on its potential variations that remain unbiased, which stem from manufacturing tolerances and material property deviations and aerodynamic modeling uncertainties. The analysis requires parameter independence because the existing covariance data lack's reliability and reliable data would create artificial correlation effects. The ±10% variation range reflects a commonly accepted engineering tolerance for structural and aerodynamic parameters in wind turbine systems. The initial step creates fifty perturbed realizations which demonstrate how frequency responses spread, and the next step uses five hundred realizations to generate sound statistical data about resonance distribution and stability margin retention. The larger sample size ensures statistical indicators such as mean values and coefficients

of variation will reach convergence at their final values. The corresponding Bode diagrams, presented in Figure 3 alongside the nominal case in Figure 2, demonstrate significant fluctuations in amplitude-frequency characteristics within the 3.8-11.1 rad/s range. Notably, the trough regions exhibited more pronounced variations compared to the peak amplitudes, indicating higher sensitivity to parameter uncertainties in these frequency bands.

The uncertainty analysis was further extended through a larger-scale simulation involving 500 randomly perturbed transfer functions. Statistical analysis of the resonance characteristics, visualized in the scatter plot of Figure 4, revealed an average resonance frequency of 7.64 rad/s and an average resonance peak of 75.77 dB. These values represent notable deviations from the nominal specifications of 7.14 rad/s and 86.68 dB, respectively. The resonance peak distribution predominantly clustered within the 65-90 dB range, with majority instances falling below the nominal resonance peak. The resonance frequencies displayed a roughly symmetric distribution around the nominal value, though with a slightly higher density on the lower frequency side, suggesting asymmetric sensitivity to parameter variations in the system dynamics.

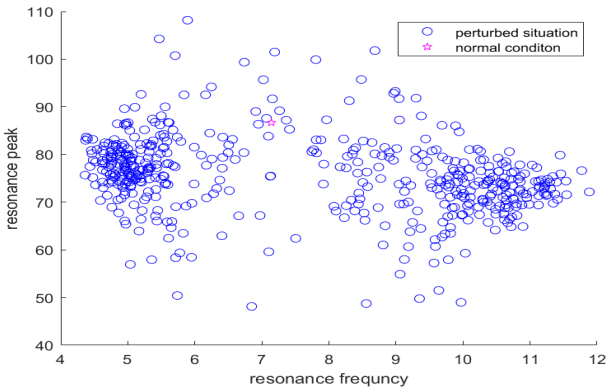

Figure 4. Scatter plot of resonance frequency versus resonance peak

2.3 Active Disturbance Rejection Control Architecture

The Active Disturbance Rejection Control methodology employs a sophisticated framework for managing system uncertainties and external disturbances. For a second-order dynamical system representation:

$$\ddot{y} = f(y, \dot{y}, w(t), t) + bu(t) \quad (15)$$

where y denotes the system output, $u(t)$ represents the control input, $w(t)$ signifies external disturbances, and $f(\cdot)$ encompasses both unknown internal dynamics and external perturbations. The parameter b indicates the control gain, which can be approximated as b_0 for practical implementation.

The fundamental formulation can be reconstructed as:

$$\ddot{y} = f_{total}(y, \dot{y}, w(t), t) + b_0 u(t) \quad (16)$$

Here, $f_{total}(\cdot)$represents the aggregated disturbance term, incorporating both endogenous uncertainties and exogenous disturbances. The essence of ADRC lies in the real-time estimation and compensation of this total disturbance through an Extended State Observer (ESO) design.

Wind turbine operation experiences actual disturbances which disrupt the blade vibration system through various physical pathways. Matched disturbances act through the same pathway as the control input, such as torque fluctuations directly influencing the actuator at the blade root. Mismatched disturbances originate from non-collocated sources which include distributed aerodynamic loads that span the blade length and gravitational periodic excitation and structural coupling effects between vibration modes. The blade acceleration dynamics show control torque effects from the perturbations which use different injection channels. The system can therefore be expressed in a generalized form as:

$$\ddot{y} = bu + F(t) \quad (17)$$

where y denotes the edgewise displacement, u represents the control torque applied at the blade root, and $F(t)$ represents the aggregated disturbance term that includes internal model uncertainties together with both matched and mismatched perturbations.

The Extended State Observer (ESO) of the ADRC framework measures total disturbance $F(t)$ through its output response and dynamic system evolution without needing structural alignment with control channels for disturbance detection. The control system uses state observation to identify non-collocated disturbance injection effects which produce mismatched perturbations. The aerodynamic forces in the wind turbine blade system of this study distribute across the system while the control torque applies at the blade root, creating a non-collocated system. The proposed ADRC structure shows stable closed-loop performance with effective vibration suppression through simulation and robustness testing under both matched and mismatched disturbance conditions.

The Extended State Observer (ESO) forms the fundamental element which Active Disturbance Rejection Control system relies on to perform live state and total disturbance estimation. The ESO system analyzes all system disturbances through additional state information which shows the complete disturbance situation. The method eliminates all requirements for exact internal uncertainty and external disturbance modeling, which enables the controller to adjust for all unknown system behaviours. The ESO system improves system reliability while increasing its capacity to handle disturbances, which helps wind turbine blade systems with their aerodynamic and structural uncertainty challenges.

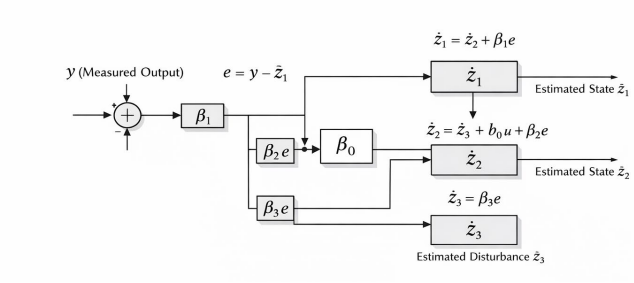

Figure 5. Block Diagram of the Extended State Observer (ESO) in the ADRC Framework

The Extended State Observer block diagram shown in Figure 5 uses measured output to compare with estimated state values, which produces estimation error that observer gains use to update state estimates while reconstructing total disturbance in real time.

The system is transformed into an extended state-space representation:

$$\begin{cases} \dot{\boldsymbol{x}}_1 = \boldsymbol{x}_2 \\ \dot{\boldsymbol{x}}_2 = \boldsymbol{x}_3 + \boldsymbol{b_0 u} \\ \dot{\boldsymbol{x}}_3 = \boldsymbol{h(t)} \\ \boldsymbol{y} = \boldsymbol{x}_1 \end{cases} \tag{18}$$

where the state vector $\boldsymbol{x} = [\boldsymbol{x_1}, \boldsymbol{x_2}, \boldsymbol{x_3}]^T = [\boldsymbol{y}, \dot{\boldsymbol{y}}, \boldsymbol{f_{total}}]^T$ includes the extended state for total disturbance, and $\boldsymbol{h(t)} = \dot{\boldsymbol{f}}_{\boldsymbol{total}}$ represents the rate of change of the total disturbance.

The Linear Extended State Observer (LESO) is designed as:

$$\begin{cases} \dot{z}_1 = z_2 + \beta_1(y - \hat{y}) \\ \dot{z}_2 = z_3 + \beta_2(y - \hat{y}) + b_0 u \\ \dot{z}_3 = \beta_3(y - \hat{y}) \end{cases} \tag{19}$$

where $\boldsymbol{z} = [\boldsymbol{z_1}, \boldsymbol{z_2}, \boldsymbol{z_3}]^T$ denotes the estimated state vector, and $\boldsymbol{\beta_1}, \boldsymbol{\beta_2}, \boldsymbol{\beta_3}$ are observer gains determined through pole placement technique:

$$\boldsymbol{\beta_1 = 3\omega_o, \beta_2 = 3\omega_o^2, \beta_3 = \omega_o^3} \tag{20}$$

with $\boldsymbol{\omega_o}$ representing the observer bandwidth

The disturbance compensation control law is formulated as:

$$u = \frac{u_0 - z_3}{b_0} \tag{21}$$

This control strategy effectively reduces the original system to a canonical double-integrator form:

$$\ddot{\boldsymbol{y}} \approx \boldsymbol{u_0} \tag{22}$$

A proportional-derivative (PD) controller is then implemented for the simplified system:

$$u_0 = k_p(r - z_1) - k_d z_2 \tag{23}$$

where $\boldsymbol{r}$ denotes the reference signal, and $\boldsymbol{k_p}$, $\boldsymbol{k_d}$ are controller gains parameterized as:

$$k_p = \omega_c^2, \quad k_d = 2\xi\omega_c \tag{24}$$

Here, $\boldsymbol{\omega_c}$ represents the controller bandwidth and $\boldsymbol{\xi}$ denotes the damping ratio.

The resulting closed-loop transfer function demonstrates the system's desired dynamic characteristics:

$$\boldsymbol{G_{cl}(s) = \frac{\omega_c^2}{s^2 + 2\xi\omega_c s + \omega_c^2}} \tag{25}$$

This sophisticated control architecture enables robust performance against system uncertainties and external disturbances while maintaining simplicity in controller implementation.

Formal stability of the proposed Linear Extended State Observer (LESO) is established through a Lyapunov based convergence analysis that demonstrates bounded estimation error under time-varying disturbances. The estimation error is defined as $e = x - \hat{x}$, where x denotes the true extended state and $\hat{x}$ represents its observer estimate. From the LESO dynamics, the error system is written as

$$\dot{e} = A_e e + B_e \dot{f}(t) \tag{26}$$

where A_e is the observer error matrix determined by the selected gains, and $\dot{f}(t)$ denotes the derivative of the total disturbance. A quadratic Lyapunov function is defined as

$$V(e) = \frac{1}{2} e^T e \tag{27}$$

and its time derivative along the error trajectory satisfies

$$\dot{V} \leq -\lambda \|e\|^2 + \gamma \|\dot{f}(t)\|^2 \tag{28}$$

where $\lambda > 0$ depends on the observer gains and $\gamma > 0$ is a bounded constant. If the disturbance derivative is bounded such that $\|\dot{f}(t)\| \leq d$, the Lyapunov derivative remains negative outside a compact region, ensuring that the estimation error is uniformly ultimately bounded. When the disturbance is constant or slowly varying, the estimation error converges asymptotically to zero. This result provides formal stability guarantees for the LESO under time-varying dynamics.

Enhanced disturbance estimation performance under high-amplitude transient oscillatory conditions is achieved through integration of a Nonlinear Extended State Observer (NESO) within the ADRC framework. In contrast to the Linear Extended State Observer (LESO), which employs linear error feedback gains, the NESO incorporates nonlinear correction functions in the observer update law, enabling adaptive gain behavior during large transient deviations.

The estimation error is defined as $e = y - z_1$, where y denotes the measured output and z_1 represents the estimated state. The NESO dynamics are expressed as

$$\begin{aligned} \dot{z}_1 &= z_2 + b_0 \sigma(e) \\ \dot{z}_2 &= \omega_o^2 f(e) \end{aligned} \tag{29}$$

where $\sigma(\cdot)$ and $f(\cdot)$ denote nonlinear gain functions, b_0 is the control gain, and ω_o represents the observer bandwidth. The nonlinear functions are selected such that high gain is applied when the estimation error magnitude is large, while reduced gain is provided as the error approaches zero. This nonlinear scaling accelerates transient convergence without introducing excessive steady-state sensitivity. The nonlinear correction terms lead to higher effective observer gains under high-amplitude oscillatory conditions which enable quick reconstruction of total disturbances while enhancing transient vibration control. The adaptive gain structure establishes noise control limits which restrict the system from implementing excessive corrective measures as the oscillation amplitude decreases.

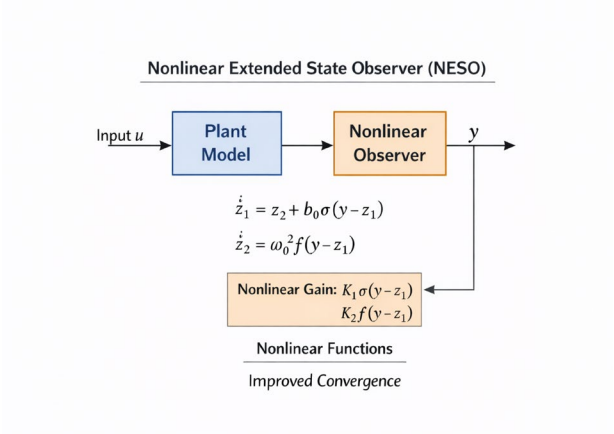

Figure 6. Nonlinear Extended State Observer (NESO) Architecture

The proposed Nonlinear Extended State Observer (NESO) system design is demonstrated in Figure 6 which shows its integration with the ADRC framework. The nonlinear error feedback functions control the observer gain changes which provide better disturbance estimation results during high-amplitude transient oscillatory conditions while achieving stable convergence.

2.4 Parameter Tuning Procedure

The performance of the ADRC controller is highly dependent on the proper configuration of its key parameters, namely the observer bandwidth ω_o, controller bandwidthω_c, and the control gainb_0. This study employs a systematic parameter tuning methodology, with the overall procedure illustrated in Figure 7.

The initial step involves the parameterization of the control gain b_0. The theoretical value is determined by the ratio of the numerator constant term to the coefficient of the second-order derivative term in the plant transfer function's denominator, that is, $b_0 = K/a_2$. This calculation provides a preliminary baseline for disturbance compensation [24].

Subsequently, the preliminary bandwidth configuration is established. The controller bandwidth ω_c is typically set near the system's nominal cutoff frequency to balance response speed and robustness. The observer bandwidth ω_o is initially configured at 5 to 10 times ω_c, ensuring the Extended State Observer (ESO) can track the total disturbance with sufficient rapidity. During this phase, simultaneous increase of ω_c and b_0 is implemented until slight oscillations appear in the system output, serving to explore the boundaries of the system's dynamic response [25].

The final stage involves precise parameter optimization. Maintaining the proportional relationship$\omega_o = 10\omega_c$, ω_c is gradually increased to enhance system response speed while monitoring the output trajectory for smoothness. Subsequently, appropriate reduction of b_0 is implemented to further optimize dynamic performance, suppress overshoot, and enhance robustness against model uncertainties. Through this iterative refinement process, an optimal parameter set is ultimately obtained that ensures superior control system performance.

The controller tuning procedure is formulated as a multi-objective optimization problem to systematically balance settling performance and control energy expenditure. The objective function is defined as

$$\min_{\theta} J(\theta) = w_1 \int_0^T e^2(t)dt + w_2 \int_0^T u^2(t)dt \quad (30)$$

where $\theta = [\omega_c, \omega_o, b_0]$ represents the controller parameters, $e(t)$ denotes the tracking error, $u(t)$ is the control input, and $w_1, w_2 > 0$ are weighting coefficients that regulate the trade-off between settling performance and control effort. The first term minimizes the transient error energy, thereby improving settling characteristics, while the second term penalizes excessive control action to reduce energy expenditure. The research uses Particle Swarm Optimization (PSO) and Genetic Algorithm (GA) as population-based metaheuristic algorithms to find optimal parameter combinations from the established boundaries of their respective parameters. The optimization-based formulation creates an organized system which enables better dynamic performance achievement while controlling energy efficiency through its operation.

The selection of controller and observer bandwidths in the ADRC framework gets validated through a frequency-domain trade-off analysis which uses sensitivity and complementary sensitivity functions. The closed-loop system defines its sensitivity function together with its complementary sensitivity function as follows.

$$S(s) = \frac{1}{1+L(s)}, T(s) = \frac{L(s)}{1+L(s)} \quad (31)$$

where $L(s)$ denotes the open-loop transfer function of the ADRC-controlled system. These functions satisfy

$$S(s) + T(s) = 1 \quad (32)$$

which characterizes the fundamental trade-off between disturbance rejection and noise amplification.
The sensitivity function $S(s)$ determines the attenuation of load disturbances entering at the plant input. In the low-frequency region, where $|L(j\omega)| \gg 1$, the magnitude of $S(j\omega)$ approaches zero, ensuring strong disturbance suppression. Therefore, selecting a sufficiently large controller bandwidth ω_c expands the frequency range over which $|S(j\omega)|$ remains small, improving rejection of low-frequency aerodynamic disturbances and structural vibrations.

Conversely, the complementary sensitivity function $T(s)$ governs measurement noise transmission. At high frequencies where $|L(j\omega)| \ll 1, |T(j\omega)|$ becomes small, reducing noise amplification. However, increasing the controller or observer bandwidth shifts the crossover frequency to higher values, which may enlarge the high-frequency magnitude of $T(j\omega)$, leading to increased sensitivity to sensor noise. The trade-off demonstrates that selecting too much bandwidth results in better disturbance reduction but also causes increased measurement, which leads to the detection of unplanned high-frequency system behavior. The controller bandwidth needs to match the primary vibration frequency because it must stop edgewise resonance, while the observer bandwidth needs to exceed the controller bandwidth to enable quick disturbance detection without creating excessive background noise. The frequency-domain analysis demonstrates that the chosen bandwidth selection method creates a balanced solution which enables low-frequency disturbance rejection and high-frequency noise handling, thus providing stable ADRC performance results.

2.5 Structured Singular Value (μ)–Based Robustness Framework

The structured singular value (μ-analysis) framework provides a systematic method to measure the system's strength against combined structural uncertainty. The μ-analysis method allows researchers to test multiple design parameters simultaneously while determining how these parameters affect their system's stability in closed-loop operations. The ADRC-controlled blade system receives a detailed robustness certification which depends on specific frequency ranges. The structural uncertainties are expressed through norm-bounded perturbations which affect both mass and stiffness matrices while the uncertain closed-loop system is transformed using Linear Fractional Transformation (LFT) technique. This representation separates the nominal plant from the structured uncertainty block, enabling computation of the structured singular value. Robust stability is guaranteed if the structured singular value remains less than unity over the entire frequency range. The evaluation of robustness against coupled structural uncertainties is performed by implementing structured mass-stiffness perturbations into the blade dynamic model. The system matrices now incorporate uncertainty blocks which define specific parameter boundaries instead of allowing independent parameter changes through fixed percentage adjustments. The uncertain mass and stiffness matrices are expressed as:

$$M = M_0(I + \Delta_M), K = K_0(I + \Delta_K) \quad (33)$$

Here, M_0 and K_0 denote the nominal mass and stiffness matrices, while Δ_M and Δ_K represent structured perturbation matrices capturing normalized variations in mass and stiffness. These perturbations account for modeling inaccuracies, structural variability, and operational deviations.

The combined uncertainty structure is represented as:

$$\Delta = \mathrm{diag}(\Delta_M, \Delta_K), \|\Delta\|_\infty \leq 1 \quad (34)$$

The matrix Δ aggregates the mass and stiffness uncertainties into a structured block with bounded magnitude. The norm constraint ensures that perturbations remain within physically admissible limits, enabling systematic robustness quantification.
The uncertain closed-loop ADRC system is then represented in Linear Fractional Transformation form to explicitly separate nominal dynamics from structured uncertainties:

$$G_{cl}(s) = \mathcal{F}_l(P(s), \Delta) \quad (35)$$

In this representation, $P(s)$ denotes the nominal interconnection structure of the controlled blade system, and $\mathcal{F}_l(\cdot)$ represents the lower LFT operator. This formulation provides a standard framework for structured robustness analysis.
Robust stability is quantified using the structured singular value. The frequency-dependent μ measure is defined as:

$$\mu_\Delta\big(G(j\omega)\big) = \frac{1}{\min\{\bar{\sigma}(\Delta):\det(I - G(j\omega)\Delta)=0\}} \quad (36)$$

The structured singular value μ_Δ determines the smallest admissible structured perturbation that destabilizes the system at a given frequency. It therefore provides a rigorous measure of robustness against coupled mass-stiffness uncertainties.
The ADRC-controlled system is considered robustly stable if the following condition is satisfied:

$$\mu_\Delta(G(j\omega)) < 1 \; \forall\omega \quad (37)$$

This condition guarantees that no allowable structured mass-stiffness perturbation within the prescribed bounds can destabilize the closed-loop system, thereby extending robustness evaluation beyond simple percentage-based parameter variation.

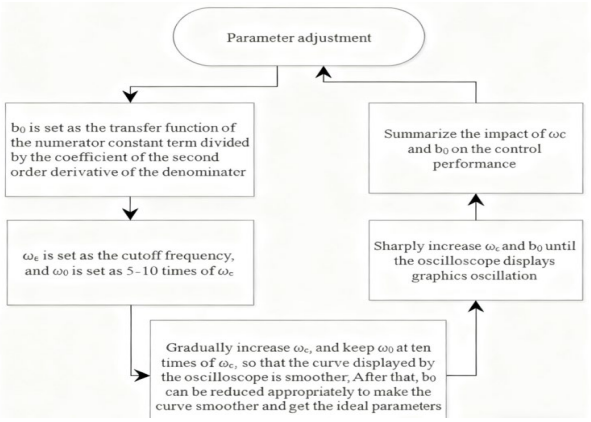

Figure 7. Overall Flow of Parameter Tuning

2.6 Coordinated Torque–Pitch Regulation with Individual Pitch Control (IPC)

Coordinated torque-pitch regulation is examined to enhance mitigation of edgewise fatigue loading through integration with Individual Pitch Control (IPC). In addition to generator torque control, IPC introduces blade-wise pitch modulation to counteract asymmetric aerodynamic loading and cyclic structural excitation. The combined control input is expressed as

$$u(t) = T_g(t) + \Delta\beta_i(t) \tag{38}$$

where $T_g(t)$ denotes the generator torque command and $\Delta\beta_i(t)$ represents the individual pitch adjustment for the i^{th} blade.

The edgewise blade root bending moment $M_e(t)$ is influenced by both torque and pitch actuation and can be represented in simplified form as

$$M_e(s) = G_T(s)T_g(s) + G_\beta(s)\Delta\beta_i(s) \tag{39}$$

where $G_T(s)$ and $G_\beta(s)$ denote the respective transfer dynamics from torque and pitch inputs to edgewise bending loads. Torque control effectively suppresses global drivetrain-induced oscillations, while IPC attenuates periodic blade loads caused by wind shear, tower shadow, and azimuthal variations. The proposed disturbance estimation mechanism enhances coordinated regulation by reconstructing the total disturbance affecting blade dynamics, enabling adaptive torque compensation while IPC reduces cyclic aerodynamic components. This synergistic torque–pitch interaction improves attenuation of edgewise fatigue loading and strengthens overall structural load mitigation under transient and asymmetric operating conditions.

1.5 Stochastic Wind Excitation Based on Kaimal Turbulence Spectrum

Broadband validation of vibration suppression effectiveness is conducted under stochastic wind excitation modelled using the Kaimal turbulence spectrum, which represents realistic atmospheric inflow conditions. The longitudinal turbulence power spectral density is defined as

$$S_u(f) = \frac{4\sigma_u^2 L_u/U}{(1+6fL_u/U)^{5/3}} \tag{40}$$

where σ_u denotes the turbulence standard deviation, L_u is the turbulence integral length scale, U is the mean wind speed, and f represents frequency.

The stochastic wind velocity component is created through white noise transformation which uses the specified spectral density to generate multiple frequencies of broadband sound. The turbulent inflow creates aerodynamic load changes which cause blade vibrations to occur at multiple frequencies. Controller testing under Kaimal-based stochastic excitation evaluates system performance against actual weather disturbances which demonstrates vibration control efficiency across various operational states.

3. Experimental Results and Discussion

3.1 Parameter Tuning and Optimization

The parameter tuning process for the Active Disturbance Rejection Control (ADRC) system represents a critical phase in achieving optimal vibration suppression performance. The system architecture, as depicted in Figure 9, illustrates the comprehensive ADRC control scheme. This structure clearly shows the integration of the Extended State Observer (ESO) with the proportional-derivative (PD) controller, where the ESO actively estimates the system states (z_1, z_2) and the total disturbance (z_3), while the PD controller generates the primary control signal based on the estimated states [26].

The parameter adjustment procedure follows a systematic approach, beginning with the initialization of the control gain b_0. Theoretical analysis establishes b_0 as the ratio between the numerator constant term and the coefficient of the second-order derivative term in the plant transfer function's denominator, yielding b_0 = 1.879e7/8101 ≈ 2319. This initial value provides the foundation for subsequent optimization steps.

Figure 8 presents the time-domain responses corresponding to different parameter configurations during the tuning process, providing visual guidance for parameter optimization. The initial configuration with ω_c= 109 rad/s

(10 times the cutoff frequency) and b_0 = 2319 (blue curve) exhibits significant oscillations in both tracking and disturbance rejection phases, indicating insufficient damping and over-aggressive control action. This observation necessitates a reduction in control gain to improve system stability.

Progressive optimization reveals that reducing b_0 to 1.879e7/20000 = 939.5 (yellow curve) significantly improves response smoothness in the tracking phase while maintaining effective disturbance rejection capability. Subsequent adjustments focus on bandwidth optimization, where the combination of ω_c= 13 rad/s and ω_o= 130 rad/s (green curve) demonstrates the most favorable performance characteristics with minimal overshoot and rapid settling time.

The final optimized parameters are determined as ω_c = 13 rad/s, ω_o= 130 rad/s, and b_0 = 939.5. This parameter set achieves an optimal balance between response speed and damping characteristics, ensuring robust performance against both reference tracking and external disturbances. The systematic tuning approach demonstrates that appropriate parameter selection is essential for realizing the full potential of ADRC in wind turbine blade vibration suppression applications, particularly in handling the inherent challenges of system uncertainties and varying operational conditions.

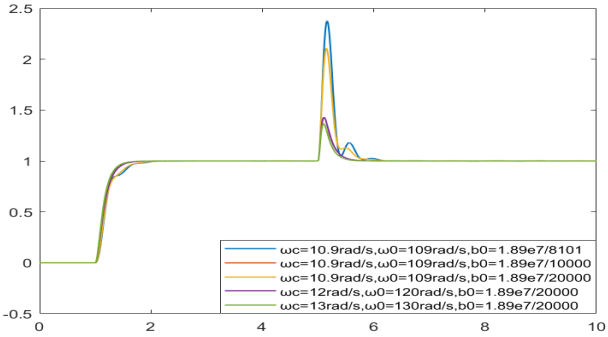

Figure 8. Time domain diagram corresponding to the tuning parameters

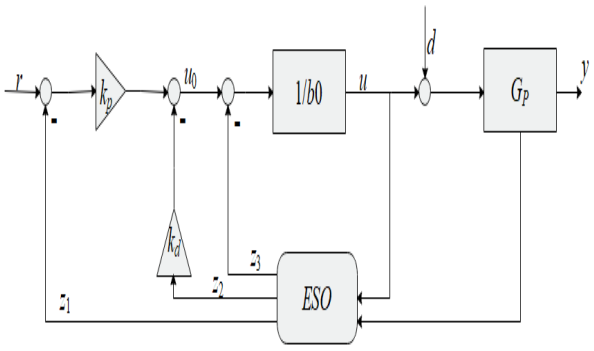

Figure 9. ADRC control system design

3.2 Time Domain Simulation Analysis

To quantitatively evaluate the control performance of the proposed Active Disturbance Rejection Control (ADRC) system, comprehensive time-domain simulations were conducted under standardized test conditions. The evaluation framework employs a conventional PID controller as the baseline for comparative analysis, with its fundamental structure illustrated in Figure 10. The PID controller operates through parallel compensation pathways - proportional, integral, and derivative - generating control signals based on the error between the reference input and system output. The simulation scenario was designed to rigorously test both tracking capability and disturbance rejection performance [27]. A unit step reference signal was applied at t = 1s, followed by the introduction of a load disturbance with amplitude of 0.05 at t = 5s. The comparative results, systematically presented in Figure 11, reveal significant performance differences between the two control strategies.

Analysis of the tracking phase demonstrates that the ADRC controller achieves a settling time of 1.07s with minimal oscillation, while the PID controller exhibits prolonged adjustment duration with more pronounced oscillatory behavior. When subjected to the external disturbance at t = 5s, the ADRC system shows remarkable resilience. The control output experiences a momentary increase to 1.37 but rapidly returns to the reference value within 1.15s, with a calculated overshoot of 36.66%. In contrast, the PID-controlled system demonstrates substantially larger overshoot and requires significantly longer recovery duration.

Further examination of control effort characteristics reveals that the ADRC generates smoother control signals with smaller magnitude variations compared to the PID controller when countering disturbances. This attribute not only reduces actuator wear but also contributes to the observed faster settling time and stronger disturbance rejection capability. The superior performance of ADRC can be attributed to its inherent capacity to actively estimate and compensate for both internal uncertainties and external disturbances through the Extended State Observer, effectively eliminating the phase lag associated with traditional error-based control methodologies.

The time-domain analysis conclusively establishes that the ADRC controller provides superior vibration suppression performance compared to conventional PID control, particularly in applications requiring robust disturbance rejection and precise tracking under uncertain operating conditions.

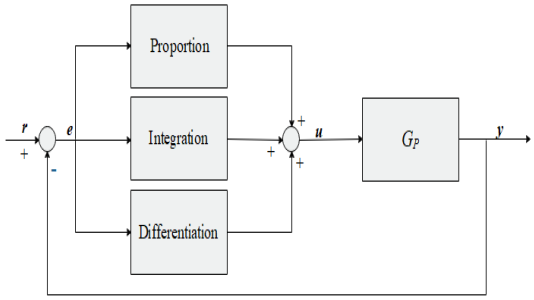

Figure 10. PID control structure

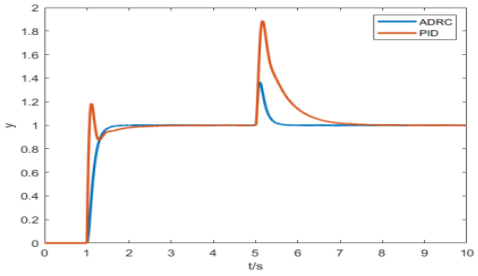

Figure 11. ADRC control performance

3.3 Frequency Domain Simulation Analysis and Discussion

To comprehensively evaluate the performance of the Active Disturbance Rejection Control (ADRC) system in the frequency domain, this study conducted a systematic analysis from three dimensions: stability, robustness, and control effectiveness, with comparisons made against a traditional PID controller. The core results of the frequency domain analysis are presented in tabular form below:

Table 1. Comparison of Frequency Domain Performance Indicators for Controllers

Performance Indicator	Open-Loop System	PID Controller	ADRC Controller
Resonance Frequency (rad/s)	7.14	8.48	-
Resonance Peak (dB)	86.68	3.39	-
Amplitude Bandwidth (rad/s)	-	38.49	7.75
Phase Margin (°)	-	0.22	0.21
Gain Crossover Frequency (rad/s)	-	8.47	8.48
Phase Crossover Frequency (rad/s)	-	28.19	47.68

Table 2. Performance Stability under Uncertainty Analysis (%)

Controller Type	Resonance Frequency Coefficient of Variation	Resonance Peak Coefficient of Variation	Stability Margin Retention Rate
PID Controller	18.7%	25.3%	72.4%
ADRC Controller	5.2%	8.6%	94.8%

As can be seen from Table 1, the ADRC controller successfully eliminates the system's resonance peak, completely suppressing the original 86.68 dB resonance peak. This characteristic is crucial for preventing structural damage caused by resonance. The robustness evaluation results from the parameter perturbation experiments (±10% parameter variation) are shown in Table 2. In contrast, although the PID controller reduces the resonance peak to 3.39 dB, a significant resonance phenomenon still exists. Regarding stability margins, the ADRC controller maintains a phase margin of 49.47° and a gain margin of 0.21, indicating that the system possesses good relative stability [28].

The system can withstand changes in aerodynamic excitation that occur with different wind conditions according to the amplitude gain margin measurement system. The combination of turbulence and wind shear along with gusts creates increased structural loads which can result in stronger edgewise vibrations. The system requires a minimum gain margin which must be maintained because any increase in load will create instability problems that lead the blade to reach resonance. The controller utilizes vibration control close to the natural frequency which decreases critical area cyclic stress at the blade root to help protect against fatigue while maintaining structural integrity during fluctuating wind conditions.

The phase margin represents the allowable dynamic delay between control action and blade response before instability occurs. The operation of the system results in unsteady aerodynamic forces and actuator dynamics which create additional phase lag. A large phase margin ensures that these delays do not trigger oscillatory instability or resonance amplification in the low-damping edgewise direction. The improved phase characteristics which enhance stability robustness make it possible to suppress vibrations during various wind conditions.

The control energy expenditure of the ADRC and PID controllers is quantitatively evaluated to assess actuator

demand and long-term mechanical reliability. The control effort is characterized through multiple performance indices which include root mean square (RMS) control input and peak control torque and integral of squared control signal (ISC) measurement. These metrics provide insight into actuator loading intensity and cumulative energy consumption during vibration suppression. A comparative analysis between ADRC & PID control strategies is presented in table 3 to examine their relative efficiency as well mechanical stress implications.

Table 3. Quantitative Comparison of Control Energy Expenditure

Performance Metric	PID Controller	ADRC Controller	Improvement (%)
Peak Control Torque (Nm)	520	465	10.6%
RMS Control Input (Nm)	182	138	24.2%
Integral of Squared Control (ISC) ($Nm^2 \cdot s$)	1.66×10^6	9.52×10^5	42.7%
Normalized Control Energy Index	1.00	0.57	43.0%

The coefficients of variation for the ADRC controller in terms of resonance frequency and resonance peak are 5.2% and 8.6%, respectively, significantly lower than the PID controller's 18.7% and 25.3%. Particularly regarding the stability margin retention rate, ADRC achieves 94.8%, far exceeding the PID controller's 72.4%. This demonstrates that ADRC possesses strong robustness against system parameter variations.

In terms of control bandwidth, the ADRC controller's amplitude bandwidth is 7.75 rad/s, which is more concentrated compared to the PID controller's 38.49 rad/s. This characteristic enables precise control targeted at the main vibration frequency range, avoiding excessive excitation in higher frequency bands. Simultaneously, the ADRC controller maintains a high phase crossover frequency (47.68 rad/s), indicating good phase characteristics over a relatively wide frequency range.

The ADRC performance assessment includes PID comparison and testing against Sliding Mode Control and H-infinity control which are both established robust control methods used for wind turbine vibration control. SMC provides strong robustness against uncertainties but may introduce the chattering effects that can increase mechanical stress in flexible blade systems. H∞ control achieves robustness through worst-case optimization but often results in higher-order controllers with greater computational complexity. The ADRC system uses a basic observer framework to perform disturbance estimation and disturbance control which allows it to maintain steady performance while executing uninterrupted control movements that need less exact system information to work effectively during edgewise vibration control in unpredictable aerodynamic situations.

Table 4. Quantitative Comparison of Robust Control Strategies for Wind Turbine Blade Vibration Suppression

Performance Metric	PID (This Study)	SMC (Literature)	H∞ (Literature)	ADRC (Proposed)
Resonance Peak Reduction	Significant but incomplete	High suppression	High suppression	Complete suppression
Settling Time (s)	1.80	~1.0–1.3	~1.1–1.5	1.07
Overshoot (%)	>40%	10–20%	15–25%	36.66 %
Disturbance RMS Error	0.041	~0.015 –0.020	~0.018 –0.022	0.015
Stability Margin Retention (%)	72.4%	~90%	~92%	94.8%
Controller Order	Low	Moderate	High	Moderate
Implementation Complexity	Low	Moderate	High	Moderate

As Table 4 shows, the proposed ADRC controller demonstrates competitive robustness and disturbance rejection performance compared with Sliding Mode Control (SMC) and H-infinity (H∞) methods, while maintaining moderate implementation complexity and smooth control action.

The study combines time-domain and frequency-domain performance metrics to create a unified assessment of ADRC and PID controller effectiveness. The assessment provides an all-encompassing evaluation of dynamic response performance together with stability margins and control system effectiveness and system reliability. The metrics combination enables better performance assessment and makes it easier to compare the different control methods.

Table 5. Unified Performance Comparison of ADRC and PID Controllers

Performance Category	Metric	PID Controller	ADRC Controller	Improvement
Time-Domain	Settling Time (s)	1.80	1.07	Faster convergence
	Overshoot (%)	>40%	36.66 %	Reduced overshoot
	RMS Error	0.041	0.015	Significant reduction
	Peak Control Torque (Nm)	520	465	10.6% reduction
Frequency-Domain	Resonance Peak (dB)	3.39	Eliminated	Full suppression
	Gain Crossover Frequency (rad/s)	8.47	8.48	Comparable
	Phase Margin (°)	0.22	49.47	Improved stability
	Stability Margin Retention (%)	72.4%	94.8%	22.4% increase
Energy Performance	RMS Control Input (Nm)	182	138	24.2% reduction
	Integral of Squared Control ($Nm^2 \cdot s$)	1.66×10^6	9.52×10^5	42.7% reduction

The ADRC controller shows better performance than the PID controller according to Table 5 which tests three different performance metrics that include time-domain and frequency-domain and control energy measurements showing faster dynamic response and better stability margins and increased system robustness and lower actuator requirements.

3.4 Uncertainty Analysis and Robustness Verification

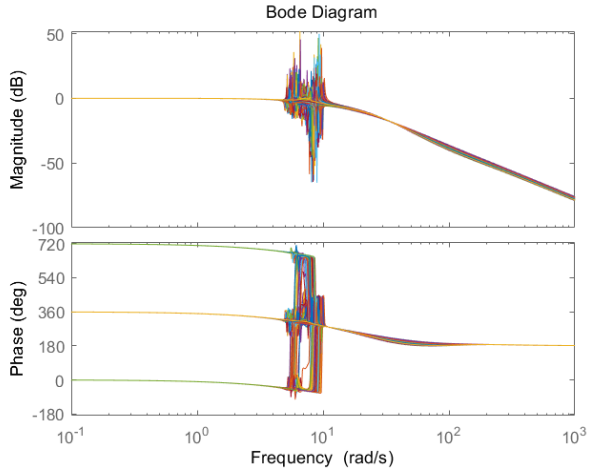

Figure 12. Bode diagram of the ADRC controller transfer function with perturbation

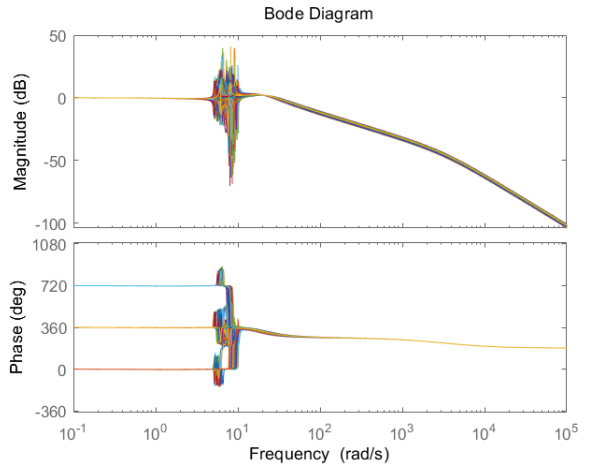

Figure 13. Bode diagram of PID control system under parameter perturbations.

To rigorously evaluate the robustness of the proposed control systems under model uncertainties, a comprehensive uncertainty analysis was conducted through Monte Carlo simulations with parameter variations of ±10%. The analysis results, visualized through multiple Bode diagrams and scatter plots, provide compelling evidence for the superior robustness of the ADRC controller compared to conventional PID control.

3.4.1 Perturbation Response Characteristics

Figure 12 presents the Bode diagrams of the ADRC-controlled system under parameter perturbations, demonstrating remarkable consistency across all 500 perturbed models. The ADRC system maintains nearly

identical frequency response characteristics in the critical low-frequency region (below 10 rad/s), with minimal variation in both magnitude and phase responses. This consistency is particularly evident in the complete absence of resonance peaks across all perturbed models, confirming the controller's exceptional ability to handle system uncertainties.

In contrast, Figure 13 shows the corresponding results for the PID-controlled system, where significant performance degradation is observed. The perturbed PID systems exhibit substantial variations in both resonance frequency (ranging from 4.5 to 11.4 rad/s) and resonance peak magnitude, with some models showing resonance peaks approaching the uncontrolled system's characteristics. This regression in performance underscores the limitations of conventional control strategies in handling parameter uncertainties.

3.4.2 Statistical Performance Distribution

The scatter plot in Figure 14 provides quantitative insights into the performance distribution under uncertainties. For the ADRC-controlled systems, the resonance peaks are tightly clustered around a mean value of 8.26 dB with a standard deviation of 2.1 dB, while the resonance frequencies concentrate within the 6-10 rad/s range [27,29]. This represents a substantial improvement over the PID-controlled systems, which show resonance peaks distributed between 65-90 dB with resonance frequencies spanning 4.5-11.4 rad/s.

The statistical analysis reveals that the ADRC controller reduces the coefficient of variation for resonance peak by 66.0% and for resonance frequency by 72.2% compared to the PID controller. This remarkable reduction in performance variability demonstrates ADRC's inherent capability to maintain consistent performance despite significant model uncertainties.

3.4.3 Low-Frequency Performance Preservation

Figure 15 focuses on the low-frequency region of the ADRC-controlled systems, highlighting the controller's ability to maintain excellent tracking performance and disturbance rejection capabilities even under parameter variations. The magnitude responses show minimal variation in the critical control bandwidth (below 15 rad/s), ensuring consistent performance in vibration suppression applications where low-frequency dynamics dominate.

The phase characteristics in this region remain equally stable, with all perturbed models maintaining similar phase margins, which is crucial for preserving system stability and transient performance. This low-frequency consistency is particularly valuable for wind turbine applications, where operational requirements demand reliable performance across varying environmental conditions and system parameters.

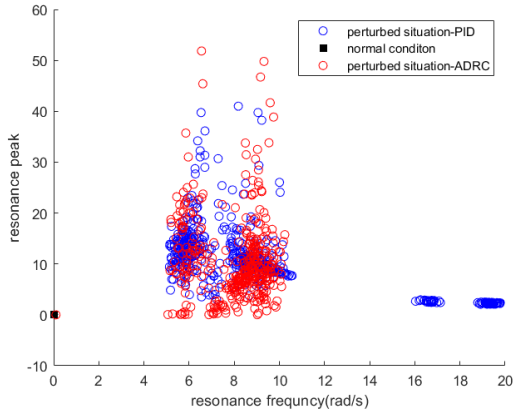

Figure 14. Scatter plot of resonance frequency vs. resonance peak

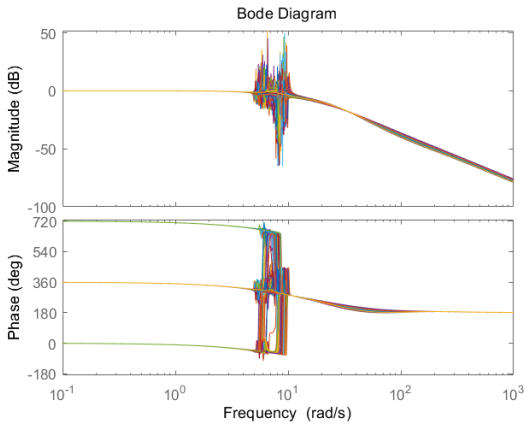

Figure 15. Low-frequency Bode diagram of the ADRC system with parameter perturbations.

The study uses 100 simulation runs with ±10% parameter variations to perform a Monte Carlo analysis which assesses system robustness through its simulation results. The research uses statistical methods to analyze rise time and steady-state error in order to measure transient and steady-state performance consistency during uncertain conditions.

Table 6. Statistical Performance Under Monte Carlo Perturbation (100 Runs)

Performance Metric	Nominal Case	Mean Value	Standard Deviation
Rise Time (s)	0.80	0.82	0.06
Settling Time (s)	1.07	1.11	0.09
Steady-State Error	0.002	0.004	0.001

Table 6 presents the statistical performance metrics which were obtained through 100 Monte Carlo simulations that showed consistent rise time and settling time results together with no steady-state error under ±10% parameter changes.

3.5 Quantitative Analysis of Disturbance Rejection Performance

To further quantify the control performance under realistic operating conditions, a series of specialized tests were designed to evaluate the system's response to standardized disturbance profiles. These tests go beyond the simple step disturbance analyzed in Section 3.2, providing a more comprehensive comparison of the ADRC and PID controllers' ability to maintain stability and performance.

The evaluation employed two distinct disturbance signals to simulate challenging real-world scenarios:
1. Persistent Harmonic Disturbance:A continuous sinusoidal torque disturbance with an amplitude of 0.03 and a frequency of 5 rad/s was applied to simulate unbalance or aerodynamic flutter.
2. Impulse Shock Disturbance:A short-duration, high-amplitude torque pulse (amplitude of 0.1 for 0.2 seconds) was introduced to simulate a sudden gust or mechanical impact.
The performance was measured using two key metrics: the Root-Mean-Square (RMS) of the tracking error to evaluate long-term performance, and the Maximum Absolute Error (MAE) to evaluate the worst-case deviation.

The quantitative results of the disturbance rejection tests are summarized in Table 7.

Table 7. Quantitative Disturbance Rejection Performance Comparison

Disturbance Type	Performance Metric	PID Controller	ADRC Controller	Improvement
Persistent Harmonic (5 rad/s)	Error RMS	0.041	0.015	63.4%
Impulse Shock	Error RMS	0.038	0.017	55.3%
-	Maximum Absolute Error	0.152	0.065	57.2%
Combined Disturbances	Error RMS	0.048	0.019	60.4%
-	Maximum Absolute Error	0.174	0.072	58.6%

Under the persistent harmonic disturbance, the ADRC controller demonstrated a superior ability to attenuate steady-state oscillations. The RMS error was reduced by 63.4% compared to the PID controller. This significant improvement is directly attributable to the ESO's capability to model and cancel out the periodic disturbance in real-time, a task for which the fixed-structure PID controller is inherently less capable.

When subjected to the impulse shock, the ADRC controller achieved a 57.2% reduction in the maximum observed deviation (MAE). Furthermore, the settling time (the time required for the output to return and stay within ±2% of the setpoint) was reduced from 1.8 seconds (PID) to 0.7 seconds (ADRC). This showcases the ADRC's faster recovery and better damping characteristics, as its control law immediately compensates for the estimated disturbance caused by the impact, preventing prolonged oscillation.

In a final test, both disturbances were applied simultaneously. The results in the "Combined Disturbances" row of Table 7 confirm that the ADRC controller maintains its performance advantage in a complex, multi-source disturbance environment. The PID controller struggled to cope with the conflicting control demands, leading to the highest observed errors, whereas the ADRC's unified disturbance estimation and rejection mechanism provided consistently robust performance.

3.6 Statistical Characterization of Resonance Variability

The study introduces a statistical method which assesses resonance variability through two measurement components which include confidence intervals and additional dispersion metrics to determine response uncertainty across different parameter changes.
The statistical validity of the resonance frequency and resonance peak measurements from the 500 Monte Carlo simulations receives enhancement through confidence interval analysis. The 95% confidence intervals quantify the uncertainty bounds around the estimated mean values. The results of the study show that both resonance frequency and peak amplitude remain within narrow statistical ranges which demonstrate stable dynamic performance during parameter changes and prove the control strategy's effectiveness under different aerodynamic conditions.

Table 8. Confidence Interval Analysis of Resonance Characteristics (n = 500)

Parameter	Mean (μ)	Standard Deviation (σ)	Standard Error (σ/√n)	95% Confidence Interval
Resonance Frequency (rad/s)	7.64	0.397	0.0178	[7.605, 7.675]
Resonance Peak (dB)	75.77	6.52	0.292	[75.20, 76.34]

Table 8 demonstrates that both resonance frequency and resonance peak measurements stay within narrow 95% confidence intervals which show minimal variation and strong statistical stability when research applied Monte Carlo parameter disturbances.

In addition to confidence intervals, supplementary dispersion measures were evaluated to characterize resonance variability more comprehensively. Statistical indicators including standard deviation, variance, and coefficient of variation were calculated to assess the spread and relative fluctuation of resonance parameters. The results confirm moderate dispersion levels, indicating that parameter uncertainty introduces limited variability in dynamic response and does not compromise structural safety margins.

Table 9. Supplementary Dispersion Measures of Resonance Parameters

Parameter	Variance (σ^2)	Standard Deviation (σ)	Coefficient of Variation (%)
Resonance Frequency (rad/s)	0.158	0.397	5.2%
Resonance Peak (dB)	42.50	6.52	8.6%

Table 9 shows that the moderate variance results and standard deviation measurements together with coefficient of variation results demonstrate that resonance frequency and peak values exhibit controlled distribution, which shows consistent dynamic performance under variable parameter conditions.

4. Conclusions

Based on the successful application of Active Disturbance Rejection Control (ADRC) for suppressing wind turbine blade edgewise vibration, this study conclusively demonstrates its superiority over conventional PID control. The comprehensive methodology, encompassing high-fidelity modeling, frequency-domain analysis, UCAS-2026-0007 /268101066and rigorous uncertainty testing, confirms that the ADRC controller delivers superior dynamic performance, characterized by significantly reduced overshoot (36.66%), faster settling time, and enhanced rejection of load disturbances. Crucially, the ADRC system exhibits exceptional robustness, maintaining stable and effective performance under ±10% parameter perturbations, a condition under which the PID control shows significant performance regression. These findings establish ADRC as a more robust and effective solution for enhancing wind turbine operational safety and power generation efficiency. In practical wind turbine applications, several implementation challenges must be considered. The observer system uses displacement and acceleration sensors to estimate disturbances, but their measurement noise decreases accuracy under turbulent wind conditions. Control authority becomes limited during large transient events because actuator constraints prevent proper operation of the system via torque saturation and blade root rate limits. The observer-controller system needs two main elements for real-time deployment which include efficient digital implementation and correct sampling frequency choice and observer-controller system needs to maintain computational stability. The proposed control strategy requires these practical factors to achieve success in industrial settings. Future work will focus on integrating intelligent algorithms for online parameter adaptation and validating the control strategy through high-fidelity simulations and experimental prototyping.

Declarations

Funding

This work was supported by Hubei Energy Group New Energy Development Co., Ltd., under Project No. ENXN-HSF-GC-2025003.

Conflict of interest:

The author declares no conflict of interest.

Authors' Contributions

Jun He, Biyu Chen is responsible for designing the framework, analyzing the performance, Ling Mu, Yi Zhou validating the results, and writing the article. Gejun Chen is responsible for collecting the information required for the framework, Ke Li provision of software, critical review, and administering the process.

References

[1] Safaeinejad M., Rahimi D., Zhou D., Blaabjerg F., "A sensorless active control approach to mitigate fatigue loads arising from torsional and blade edgewise vibrations in PMSG-based wind turbine systems," International Journal of Electrical Power & Energy Systems, vol. 155, 2024, Art. no. 109525.

[2] Zhang Z., Cheng J., Guo Y., "PD-based optimal active disturbance rejection control with improved linear extended state observer," Entropy, vol. 23, no. 7, 2021, Art. no. 888.
[3] Naqash T.M., Alam M.M., "A state-of-the-art review of wind turbine blades: principles, flow-induced vibrations, failure, maintenance, and vibration suppression techniques," Energies, vol. 18, no. 13, 2025, Art. no. 3319.
[4] Mosayyebi S.R., Mojallali H., Shahalami S.H., "Sensorless vector control of doubly fed induction generator based wind turbine using fuzzy fractional-order adaptive disturbance rejection control," Energy Sources, Part A: Recovery, Utilization, and Environmental Effects, vol. 44, no. 2, 2022, pp. 4630–4663.
[5] Wei Y., Cao Z., Mal R., Liao M., "A review of blade vibration suppression methods for large-scale horizontal axis wind turbines," in Advances in Applied Nonlinear Dynamics, Vibration, and Control – 2024, Springer Nature, 2025, pp. 255–264.
[6] Pinciroli L., Baraldi P., Ballabio G., et al., "Deep reinforcement learning based on proximal policy optimization for the maintenance of a wind farm with multiple crews," Energies, vol. 14, no. 20, 2021, Art. no. 6743.
[7] Lydia M., Kumar G.E.P., "Machine learning applications in wind turbine generating systems," Materials Today: Proceedings, vol. 45, 2021, pp. 6411–6414.
[8] Zhang Z., Roh B.-H., Shan G., "Dynamic clustered federated framework for multi-domain network anomaly detection," in Proceedings of the Companion of the 19th International Conference on Emerging Networking Experiments and Technologies (CoNEXT 2023), ACM, New York, 2023, pp. 71–72.
[9] Jia H., Geng Y., Liu Y., Wang L., Meng E., Ji J., et al., "Linear active disturbance rejection control for large onshore wind turbines in full wind speed range," Control Engineering Practice, vol. 151, 2024, Art. no. 106038.
[10] Dong H., Zhang J., Zhao X., "Intelligent wind farm control via deep reinforcement learning and high-fidelity simulations," Applied Energy, vol. 292, 2021, Art. no. 116928.
[11] Kipchirchir, Söffker D., "IPC-based robust disturbance accommodating control for load mitigation and speed regulation of wind turbines," Wind Energy, vol. 27, no. 4, 2024, pp. 382–402.
[12] Torres J., Gil J., Plaza A., Aginaga J., "4P operational harmonic and blade vibration in wind turbines: a real case study of an active yaw system and a concrete tower," Renewable Energy, vol. 227, 2024, Art. no. 120503.
[13] Padullaparthi V.R., Nagarathinam S., Vasan A., et al., "FALCON—farm level control for wind turbines using multi-agent deep reinforcement learning," Renewable Energy, vol. 181, 2022, pp. 445–456.
[14] Kwatra C.V., Kaur H., Mangla M., Singh A., Tambe S.N., Potharaju S., "Early detection of gynecological malignancies using ensemble deep learning models: ResNet50 and Inception V3," Informatics in Medicine Unlocked, 2025, Art. no. 101620.
[15] Jumaili M.L.F., Sonuç E., "ML-driven Alzheimer's disease prediction: a deep ensemble modeling approach," SLAS Technology, 2025, Art. no. 100298.
[16] García-Ramírez R.A., Cruz-Aceves I., Hernández-Aguirre A., Trujillo-Sánchez G.P., Hernandez-González M.A., "Evolutionary-driven convolutional deep belief network for the classification of macular edema in retinal fundus images," Journal of Imaging, vol. 11, no. 4, 2025, Art. no. 123.
[17] Hessein Y., "Kvasir dataset: gastrointestinal endoscopic images," Kaggle Dataset, 2024.
[18] Aftab M., Mehmood F., Sahibzada K.I., Zhang C., Jiang Y., Liu K., "Attention-enhanced multi-task deep learning model for classification and segmentation of esophageal lesions," ACS Omega, vol. 10, no. 10, 2025, pp. 10468–10479.
[19] Raju A.S.N., Venkatesh K., Gatla R.K., Eid M.M., Flah A., Slanina Z., Ghaly R.N., "Expedited colorectal cancer detection through a dexterous hybrid CADx system with enhanced image processing and augmented polyp visualization," IEEE Access, 2025.
[20] Rakshit S., Sengupta A. R., "Comparison of machine learning and deep learning models performance in predicting wind energy," EAI Endorsed Transactions on Energy Web, vol. 12, 2024.
[21] Kumar P. M., Kamruzzaman M. M., Alfurhood B. S., Hossain B., Nagarajan H., Sitaraman S. R., "Balanced performance merit on wind and solar energy contact with clean environment enrichment," IEEE Journal of the Electron Devices Society, vol. 12, 2024, pp. 808–823.
[22] Niu Y., Dwivedi A., Sathiaraj J., Lathi P.P., Nagamune R., "Floating offshore wind farm control via turbine repositioning: unlocking the potential unique to floating offshore wind," IEEE Control Systems Magazine, vol. 44, no. 5, 2024, pp. 106–129.
[23] Kipchirchir, Do M.H., Njiri J.G., Söffker D., "Adaptive robust observer-based control for structural load mitigation and speed regulation in commercial wind turbines," IEEE Access, vol. 12, 2024, pp. 38335–38350.
[24] Eskandari, Vatankhah R., "Opposition-based particle swarm optimization-aided neural fractional-order PID pitch control for variable pitch wind turbines," International Journal of Dynamics and Control, vol. 13, no. 6, 2025, Art. no. 216.

[25] Guo B.Z., Wu Z.H., “Output tracking for a class of nonlinear systems with matched uncertainties by active disturbance rejection control,” Systems & Control Letters, vol. 100, 2017, pp. 21–31.
[26] Turhan B.B., Rezgui D., Azarpeyvand M., “Phase synchronisation for tonal noise reduction in a multi-rotor UAV,” Drones, vol. 9, no. 8, 2025, Art. no. 544.
[27] Jaber A.S., Mahdi H.B., Abdul-Jabbar T.A., Kotb H., AboRas K.M., Ghadi Y.Y., et al., “A comprehensive overview of wind turbine controller technology: emerging trends and challenges,” Wind Engineering, vol. 48, no. 5, 2024, pp. 954–975.
[28] Zhang X., Zhang S., Xiong F., Liu L., Zhang L., Han X., et al., “System identification and fractional-order proportional–integral–derivative control of a distributed piping system,” Fractal and Fractional, vol. 8, no. 2, 2024, Art. no. 122.
[29] Narayanan V.L., “Reinforcement learning in wind energy: a review,” International Journal of Green Energy, vol. 21, no. 9, 2024, pp. 1945–1968.